Heliyon 11 (2025) e42426

Contents lists available at ScienceDirect

Heliyon

journal homepage: www.cell.com/heliyon

Research article

Fabrication and performance analysis of ZnO/Ge/porous Si photodetectors for near-infrared detection

Mazin Mohd Qasim Mogdad [a], Azhar Abdul Rahman [a,*], Naser M. Ahmed [b,**], Suvindraj Rajamanickam [c], Munirah A. Almessiere [d,e]

[a] School of Physics, Universiti Sains Malaysia, Penang, 11800, Malaysia
[b] Department of Laser and Optoelectronics Engineering, Dijlah University College, Baghdad, Iraq
[c] Institute of Nano Optoelectronics Research and Technology (INOR), Universiti Sains Malaysia, USM, 11800, Penang, Malaysia
[d] Department of Biophysics, Institute for Research & Medical Consultations (IRMC), Imam Abdulrahman Bin Faisal University, P.O. Box 1982, 31441, Dammam, Saudi Arabia
[e] Department of Physics, College of Science, Imam Abdulrahman Bin Faisal University, P.O. Box 1982, 31441, Dammam, Saudi Arabia

ARTICLE INFO

Keywords:
Detector
NIR
Ge
Nanoparticles
Laser ablation
ZnO

ABSTRACT

This paper reports on the fabrication of zinc oxide (ZnO)/germanium nanoparticles (Ge NPs)/porous silicon (PSi) photodetector for near-infrared (NIR) detection. Ge NPs are synthesized via pulsed laser ablation in liquid (PLAL) followed by spray coating onto the porous Si substrate and subsequent deposition of a ZnO layer. Field emission scanning electron microscopy (FESEM) confirms the presence of Ge NPs, along with the formation of Ge microwires and a mesh-like Ge pattern on the porous Si surface, attributed to Ge NP supersaturation during spray coating. Ge NPs act as a source of photogenerated electrons, transferring them to the ZnO layer. Additionally, the Ge microwire network facilitates barrier-dominated conduction, further contributing to the generation and transfer of photogenerated electrons. The device achieves its best performance at a bias voltage of 6 V under illumination with 805 nm light, a light intensity of 1.44 mW cm^2, and a switching frequency of 6.5 Hz and responsivity of 0.16 A W^{-1}.

1. Introduction

Infrared (IR) photodetectors play an increasing role in applications ranging from night vision and thermal imaging to environmental monitoring and medical diagnostics [1]. The pursuit of high-performance IR detectors continues to drive research efforts, with a focus on enhancing sensitivity, responsivity, and spectral range. A subset of IR detection is Near-Infrared (NIR), which is more advantageous in penetrating bones, skin, and tissues due to the low scattering effect from its longer wavelength compared to visible light. NIR is typically divided into two spectral regions: NIR-I (760–1000 nm) and NIR-II (1000–1700 nm) [2]. NIR detection can thus be utilized for optoelectronic applications and has potential in solar harvesting. Following this school of thought, using new materials and creative fabrication techniques that are of low cost holds great promise for advancing NIR detection technology [3]. Porous silicon (PSi) are great platform for research into photodetectors, primarily because it is a matured technology, as much of its strength and shortcomings related to it have been well studied, and also ease of supply [4]. PSi by its rough morphology also does not require an

* Corresponding author.
** Corresponding author.
E-mail addresses: arazhar@usm.my (A.A. Rahman), nas_tiji@yahoo.com (N.M. Ahmed).

https://doi.org/10.1016/j.heliyon.2025.e42426
Received 28 October 2024; Received in revised form 30 January 2025; Accepted 31 January 2025
Available online 31 January 2025

anti-reflective coating that is very important for use as photodetectors and solar cells [4,5]. PSi also boasts strong absorption, a large surface area-to-volume ratio, and roughness control based on etching parameters [5,6]. Despite its strengths, PSi photodetectors can be further enhanced with the incorporation of nanoparticles (NPs).

NPs are making breakthroughs in optoelectronic devices due to their unique properties. Among them is its larger surface area to volume ratio compared to their bulk counterparts and quantum confinement effects that could increase the bandgap of some semiconductor materials [7]. PSi photodetectors have been researched in tandem with NPs such as titanium oxide (TiO_2) [6], copper oxide (CuO) [8], and cadmium sulphide (CdS) [9], among others. Researchers also put focus on II-VI Cd-based [10], IV-VI lead (Pb)-based [11], III-V Indium (In) [12], and gallium (Ga)-based compound quantum dots [13] as they can undergo wavelength tuneable emission, strong absorption to incident light and long electron-hole recombination lifetime. Despite that, they are considered heavy metals and toxic by nature, and future research requires a safer approach to sustainability efforts [7]. Among some good alternatives are silicon (Si) and germanium (Ge). Ge NPs have a higher excitonic Bohr, radius (11.5 nm), and narrower bandgap (0.67 eV) compared to Si (4.9 nm and 1.12 eV), allowing Ge to have more quantum confinement effects and a larger spectral range to encompass the NIR range (760–1700 nm), an excellent material for NIR photodetectors and emitters [7,14].

Ge NPs also have some drawbacks, primarily the method of synthesis that requires high-temperature and sophisticated processes such as molecular beam epitaxy and radio-frequency (RF) sputtering [15]. Therefore, a simpler method is employing the sol-gel method or laser ablation. Sol-gel methods have the limitation of not obtaining sufficient and uniform highly crystalline monodisperse Ge NPs for starting precursors [16]. Another easy method is by pulsed laser ablation in liquid (PLAL) from bulk targets [15]. Utilizing laser ablation in liquids allows synthesis at room temperature. Furthermore, precise control over NP properties is attainable through fine-tuning liquid and laser parameters [15].

The utilization of zinc oxide (ZnO) in combination with Ge is also done as ZnO has many benefits. Among them is the versatility of ZnO, as it is created using wet methods such as chemical bath deposition and the hydrothermal method and physical methods such as physical vapor deposition (PVD), molecular beam epitaxy (MBE), pulsed laser deposition (PLD), and sputtering [17]. ZnO is an excellent material for optoelectronic applications, such as having a wide bandgap (3.37 eV), and large exciton binding energy (60 meV), and is usually employed for photodetectors [18–20]. In addition to that, ZnO can be processed into many nanostructures and is environmentally safe [17,21]. The ZnO layer serves as a protective and stabilizing agent for the Ge NPs, ensuring their longevity, integrity, and performance in the photodetection application while potentially offering additional optical benefits, as Ge is easily oxidised when exposed to oxygen and water [22].

Due to the attractive properties of all three materials (Porous Silicon, Ge, and ZnO), a research idea occurs to study their

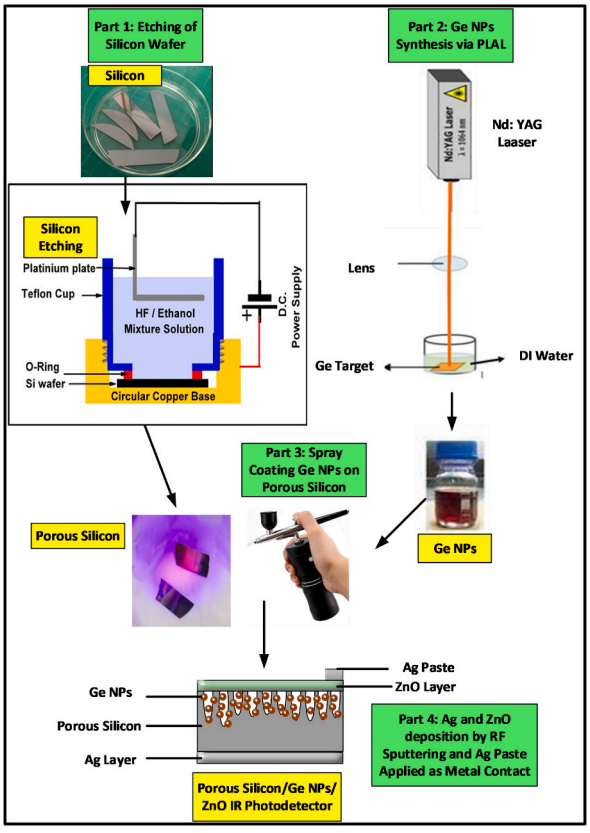

Fig. 1. Experimental procedure and schematic diagram of PSi/Ge NPs/ZnO NIR Photodetector.

combination for the synthesis and characterization of photodetectors. In this paper, we report a novel NIR photodetector consisting of a PSi layer incorporated with Ge NPs that is synthesized via the PLAL method and finally, covered with a layer of ZnO deposited via RF sputtering. This method provides an easy, low-cost method to fabricate near-infrared photodetectors utilizing both ZnO and Ge. To test the performance of the NIR photodetector, we used an 805 nm monochromatic light source from a light-emitting diode (LED)

2. Experimental procedure

The experimental procedure consisted of three parts. The first part is the synthesis of porous silicon (PSi) via etching of silicon wafers. Electrochemical etching is a common method for PSi synthesis using a platinum plate as the cathode and the silicon wafer functions as the anode. The silicon wafer is then immersed in a hydrofluoric acid (HF)/ethanol mixture solution. A constant current (20 mA) flows through the anode, to the solution and finally connects to the cathode for 20 min. The second part is the synthesis of the Ge NPs via Pulsed Laser Ablation in Liquid (PLAL). In this study, the PLAL was conducted in deionized water (DI) and performed using high-powered laser pulses with a wavelength of 1064 nm and a pulse duration of 10 ns. The energy of the laser radiation was optimized to be 250 mJ and the number of pulses was 500 pulses. The estimated spot size or the focal of the focusing lens for the PLAL experiment is 0.5 mm. The third part is the spray-coating of Ge NPs into the PSi. In the final part, a ZnO layer was deposited on the PSi substrate via RF sputtering (Auto 500 Edwards) to form the ZnO/GeNPs/PSi, after being spray coated with Ge NPs.

Morphological analysis of the samples is analyzed using the Field Emission Scanning Electron Microscope (FESEM- FEI Nova Nano SEM 450). Energy Dispersive X-ray (EDX) spectroscopy analysis is conducted in situ with FESEM analysis. Current-voltage (I-V) and current-time (I-t) measurements are carried out using a Keithley 2400 system setup. The light source used in the photodetector testing is a monochromatic light source utilizing an LED of wavelength 805 nm. The photodetector testing is done at room temperature of 25 °C. Fig. 1 shows the schematic diagram of the experimental setup.

3. Results and discussion

3.1. Morphological study

Fig. 2 shows the FESEM images of Ge NPs decorated with a ZnO layer deposited by RF sputtering. EDX spectrum of the FESEM image was obtained, with the atomic and weight spectra provided. As can be seen in the FESEM image of lower magnification (Fig. 2 (a)), there is the appearance of fiber-like morphology, with an average diameter of 0.8–1.0 μm. These fibers are attributed to Ge and previous researchers have noted the ability of Ge NPs to form Ge nanofibers. As proposed by Mingyuan et al., during the spray-coating of Ge NPs onto the porous Si wafer, small Ge NPs would aggregate into larger Ge NPs. These larger Ge NPs would then solidify and

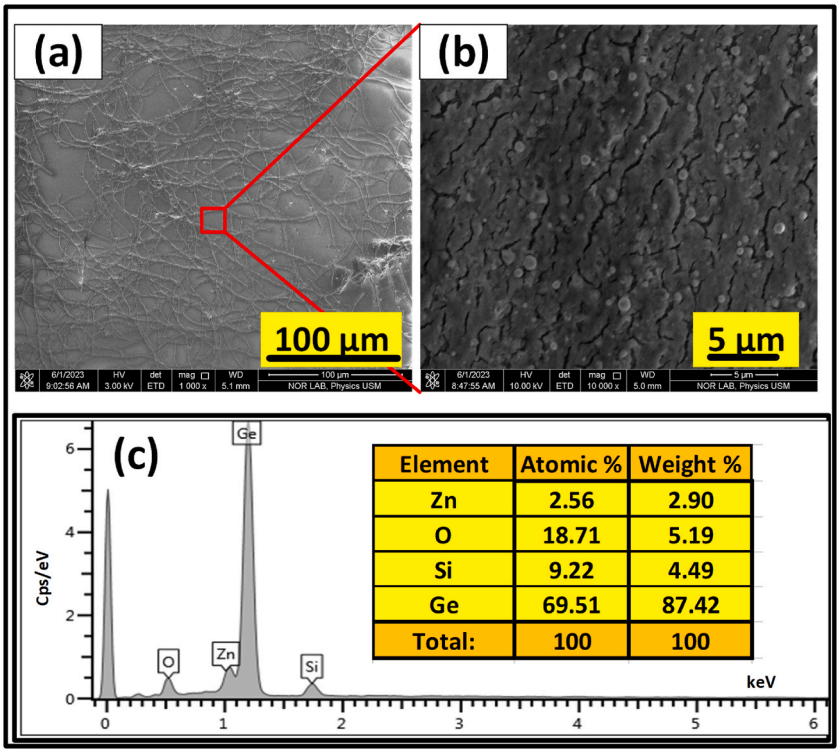

Fig. 2. (a) FESEM image of PSi/Ge NPs/ZnO, (b) magnified FESEM image, and (c) EDX spectrum of the FESEM image.

become "self-catalysts" for the formation of Ge nanowires [23]. It should be noted that Mingyuan et al. mentioned an intermediary state of cubic Ge NPs, prior to the formation of the nanowires. However, in this work, it was deduced that there were no cubic Ge NPs due to the nanowires not having a cubic shape, suggesting the growth of nanowires would still occur. Once smaller Ge NPs are in contact with larger Ge NPs, the [110] direction is the preferred choice for further growth, in lower temperatures [23]. Another research was done by Gu et al. and they also concluded that the growth of Ge nanowires can grow from liquid droplets of Ge NPs due to the supersaturation of Ge NPs present [24].

They also noted that the diameter of their Ge nanowires can be adjusted via the concentration of the precursor material [23]. In our case, with the observance of large diameter Ge microwires (0.8–1.0 μm), the amount of Ge NPs spray-coated was substantial. Furthermore, it appears that some of the microwires form a mesh-like pattern. A larger magnification of the FESEM image, shown in Fig. 2 (b), illustrates the Ge NPs present in the sample, with the largest observed having a diameter of roughly 1 μm. This can also suggest the growth of the Ge NPs from smaller ones. The EDX spectrum of the sample, as shown in Fig. 2 (c), was provided to support our assertion. ZnO makes up roughly 20 % of the atomic weight detected, with Zn and O contributing 2.56 and 18.71 % respectively. The detection of a strong presence of O could indicate that Ge NPs are subjected to oxidation since the spray coating process was not conducted in a vacuum. Si contributes a mere 9.22 % to the total atomic weight whereas the majority detected is due to Ge, at 69.51 %. Therefore, the coating of ZnO provided a small layer covering the Ge microwires and NPs.

3.2. NIR photodetector performance

3.2.1. Current-voltage (I-V) characteristics

Fig. 3 shows the I-V plot of the PSi/Ge NPs/ZnO NIR Photodetector under dark and 805 nm illumination. The device appeared to show photoresponse at 1.12 V. The photodetector showed photoresponse under NIR illumination, obtaining a photocurrent of 3.30×10^{-5} A against a dark current of 1.85×10^{-5} A at 5 V bias voltage. This gives the photodetector a gain of approximately 1.78.

3.2.2. Current-time (I-t) characteristics

Fig. 4(a–d) shows the I-t graphs of PSi/Ge NPs/ZnO NIR Photodetector under 805 nm illumination of various intensities at 2 V bias with 2, 3.5, 5, and 6.5 Hz switching mode. Fig. 5(a–d) shows the I-t graphs the photodetector under 805 nm illumination of various intensities at 4 V bias with 2, 3.5, 5, and 6.5 Hz switching mode. Lastly, Fig. 6(a–d) shows the I-t graphs of the photodetector under 805 nm illumination of various intensities at 6 V bias with 2, 3.5, 5, and 6.5 Hz switching mode. The various intensities tested are 0.377, 0.714, 1.030, and 1.440 mW cm^{-2}. Some of the I-t patterns appear truncated/cut as they are cut at fixed durations to fit them all in one subgraph. This was also done without shifting the patterns vertically to preserve the dark/photocurrent values.

Another important point to note is that the dark current levels for all I-t patterns observed in Figs. 4–6 show a slight increase, as the illumination intensity increases. This can be attributed to the persistent photoconductivity (PPC) effect which in turn is due to trap states present in the photodetector, either from ZnO, PSi, or Ge [25]. However, at 1.440 mW cm^{-2} intensity, the dark current level shows a minimal increase over time, signifying that the PPC effect is minimal, possibly after the photodetector has reached its saturation limit. This is further supported by the observation that the photocurrent did not increase greatly when the intensity increased from 1.030 to 1.440 mW cm^{-2}.

The general observation is that the photocurrent increases as the light intensity increases. For 2 V bias voltage, the photocurrent ranged from 1.0×10^{-5} A at the lowest intensity to approximately 2.2×10^{-5} A at the highest intensity. For the 4 V bias voltage, the photocurrent ranged from 2.7 to 4.14×10^{-5} A whereas for the 6 V bias voltage, the photocurrent ranged from 4.4 to 7.0×10^{-5} A. This shows the increase of photocurrent detected due to increased bias voltage which can be influenced by the increase in dark current.

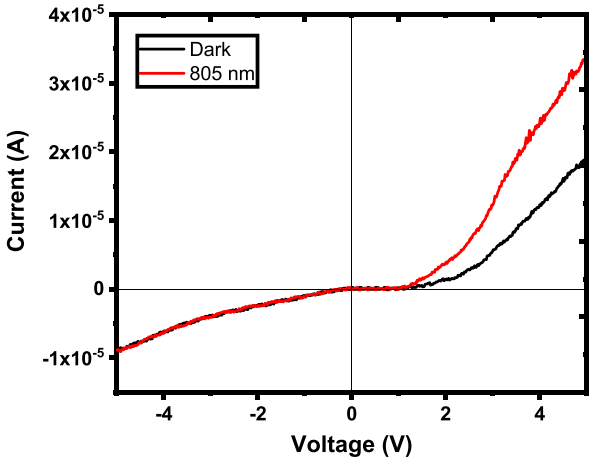

Fig. 3. I-V plot of PSi/Ge NPs/ZnO NIR Photodetector under dark and 805 nm illumination.

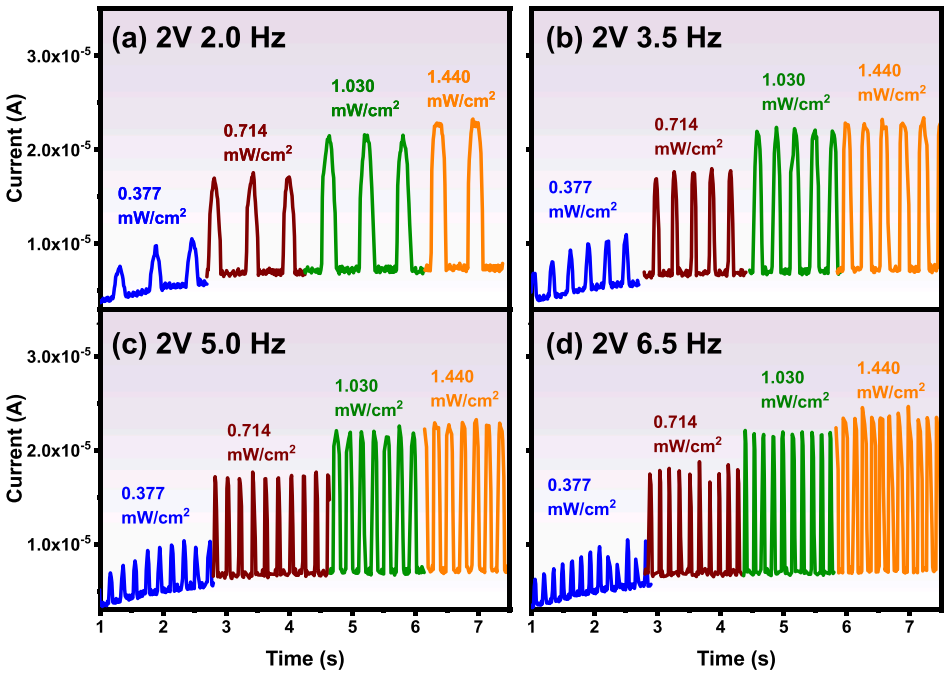

Fig. 4. I-t graphs of PSi/Ge NPs/ZnO NIR Photodetector under 805 nm illumination of various intensities at 2 V bias with (a) 2, (b) 3.5, (c) 5, and (d) 6.5 Hz switching mode.

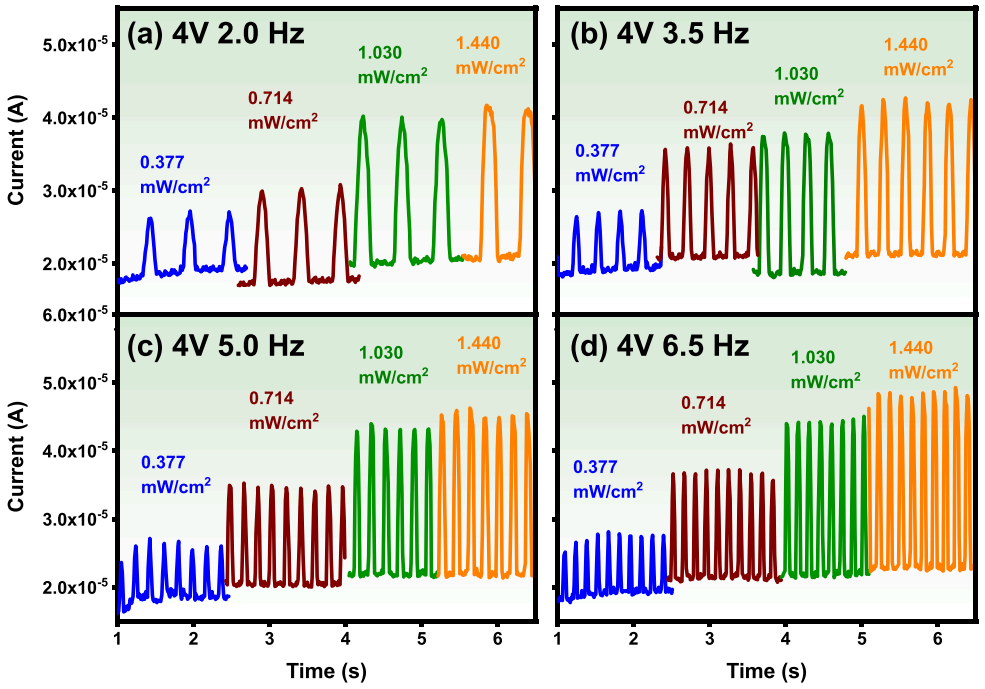

Fig. 5. I-t graphs of PSi/Ge NPs/ZnO NIR Photodetector under 805 nm illumination of various intensities at 4 V bias with (a) 2, (b) 3.5, (c) 5, and (d) 6.5 Hz switching mode.

3.2.3. Analysis

Further analysis of the photodetector was conducted by calculating the photodetector's figures of merit. Some of the figures of merit that were calculated are Sensitivity, Responsivity, and External Quantum Efficiency (EQE). Sensitivity compares the ratio of current generated due to light absorption (photocurrent) to the current flowing in the absence of light (dark current). Responsivity, on

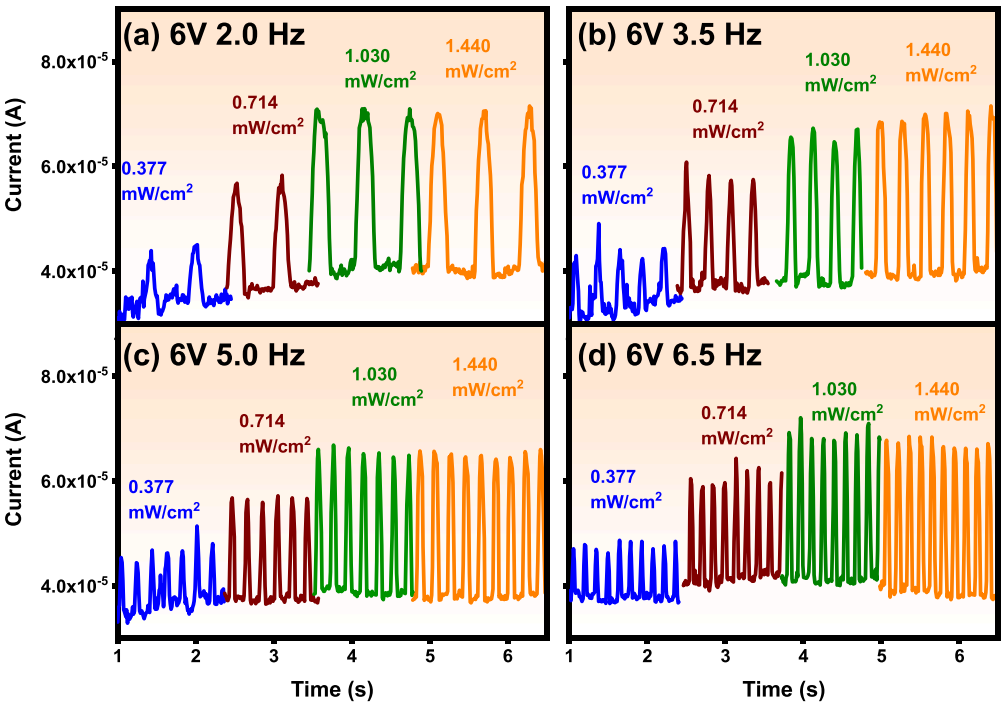

Fig. 6. I-t graphs of PSi/Ge NPs/ZnO NIR Photodetector under 805 nm illumination of various intensities at 6 V bias with (a) 2, (b) 3.5, (c) 5, and (d) 6.5 Hz switching mode.

the other hand, relates the output current (the signal) to the incoming light power. This light power is calculated by multiplying the illumination intensity by the photodiode's active area (0.5 cm^2). Finally, external quantum efficiency expresses the ratio of collected charge carriers within the photodiode to the number of photons that strike it. The mathematical formulas used to calculate these parameters are presented below in equations (1)–(3), along with that defines the symbols used as tabulated in Table 1 [26–28]:

$$S\% = \frac{I_{light} - I_{dark}}{I_{dark}} \times 100\% \tag{1}$$

$$R = \frac{I_{light} - I_{dark}}{P_{opt}} \tag{2}$$

$$EQE\ (\%) = \frac{Rhc}{q\lambda} \times 100\% \tag{3}$$

Fig. 7(a–c) shows the sensitivity values for the photodetector under 2, 4, and 6 V bias voltage, plotted with 2–6.5 Hz switching speed and 0.377–1.440 mW cm^{-2} intensities. The general trend shows the sensitivity values decrease as the bias voltage increases, for all intensities and switching speeds. At 2 V bias voltage, the sensitivity ranged from 80 to 220 %, reducing to 25–100 % for 4 V and lastly, 30–80 % for 6 V. The decrease in sensitivity occurs due to the increase in dark current as the bias voltage increases, correlated as in Equation (1).

If the bias voltages are fixed, higher illumination intensity corresponds to higher sensitivity. This is due to higher photogenerated electrons being created from higher illumination intensity [29]. With a fixed bias voltage, the depletion region stays the same width

Table 1
List of symbols with their respective meanings.

Symbol	Meaning
I_{dark}	Current measured under dark condition (A)
I_{light}	Current measured under illumination (A)
P_{opt}	Incident illumination power (W)
A	Effective area of the photodiode (cm^2)
q	Electron charge
h	Planck's constant
c	Speed of light
λ	Wavelength of light (nm)

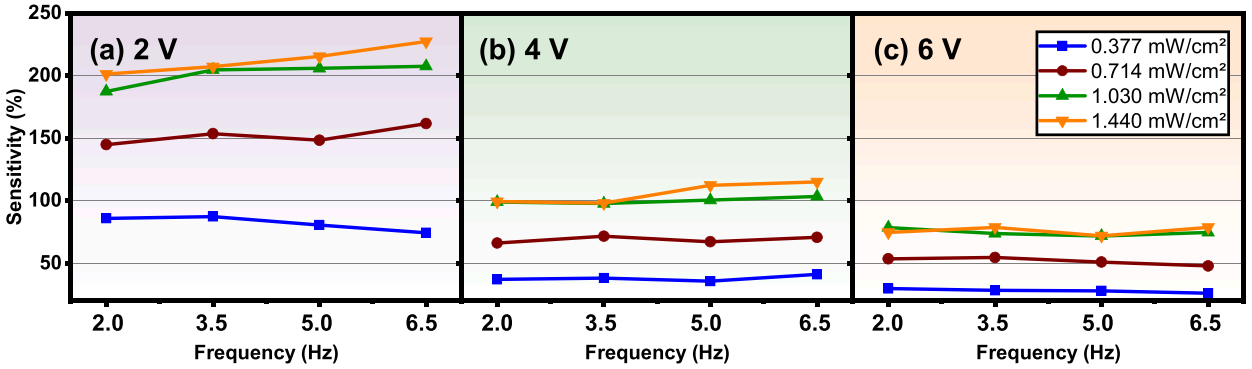

Fig. 7. Sensitivity values for PSi/Ge NPs/ZnO NIR Photodetector under (a) 2, (b) 4, and (c) 6 V bias voltage.

and thus dark current effect should be constant. With fixed bias voltage and illumination intensity, there does not appear to be any changes in the sensitivity values as the switching speed increases.

Fig. 8(a–c) shows the Responsivity values for the photodetector under 2, 4, and 6 V bias voltages. The general trend is different compared to sensitivity values, whereby the increase in bias voltage increased Responsivity values. For 2 V bias voltage, the responsivity ranges from 0.02 to 0.03 A W^{-1}. For 4 V, it ranges from 0.02 to 0.10 A W^{-1} and 0.03–0.16 A W^{-1}. Despite the general trend, there are some outlier results such as the device obtaining very high responsivity at 0.10 A W^{-1} for 4 V, 1.030 mW cm^{-2}, and 0.16 A W^{-1} at 6 V, 1.440 mW cm^{-2}.

At fixed bias voltages, a higher illumination intensity does not necessarily correspond to a higher responsivity. For example in 2 V bias voltage, the device under 1.440 mW cm^{-2} illumination recorded the lowest Responsivity values among the four illuminations tested. Despite that, at 6 V bias voltage, it recorded 0.16 A W^{-1}, the highest recorded.

The reason why the increase in responsivity occurs when the bias voltage increases is because the bias voltage increases the electric field around the depletion width of the photodetector, which in turn increases the depletion width, allowing more area for light absorption into photogenerated electron-hole pairs. Furthermore, the stronger electric field gives a stronger "pull" of the photo-generated electron-hole pairs into their respective electrodes.

Not only that, but a stronger electric field within the depletion region also enhances the drift velocity of the free carriers present in it, either created by light or thermally generated. The drift velocity of the free carriers is related to bias voltage by the equation [30]:

$$v = -\mu E \tag{5}$$

whereby v is the drift velocity of the carrier (in this case electrons), μ is the electron mobility and E is the electric field present.

To address why 1.440 mW cm^{-2} recorded lower responsivity values, equation (2) shows that Responsivity is inversely proportional to optical power, and a higher photocurrent and dark current does not appear to improve responsivity values significantly, with the exception of outlier results presented earlier. The increase in switching speed also does not alter the responsivity results greatly, showing the device being stable in delivering fixed performance.

The EQE values are graphed in Fig. 9(a–c), which shows the EQE values for the photodetector under 2, 4, and 6 V bias voltages. The trend of EQE closely follows Responsivity as EQE is closely related to Responsivity as shown in (4) for same wavelength illumination.

Fig. 10(a–c) shows the rise time for the photodetector under 2, 4, and 6 V bias voltage, plotted with 2–6.5 Hz switching frequency and 0.377–1.440 mW cm^{-2} intensities. The rise time is defined as the time needed for the photocurrent to increase from 10 to 90 % of its maximum photocurrent during the illumination stage. Conversely, the fall time is defined as the time taken for the photodetector

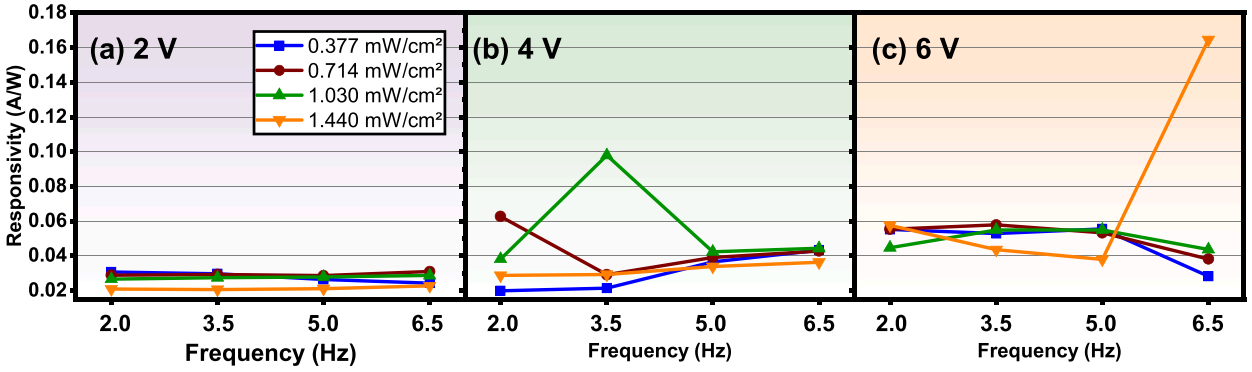

Fig. 8. Responsivity values for PSi/Ge NPs/ZnO NIR Photodetector under (a) 2, (b) 4, and (c) 6 V bias voltage.

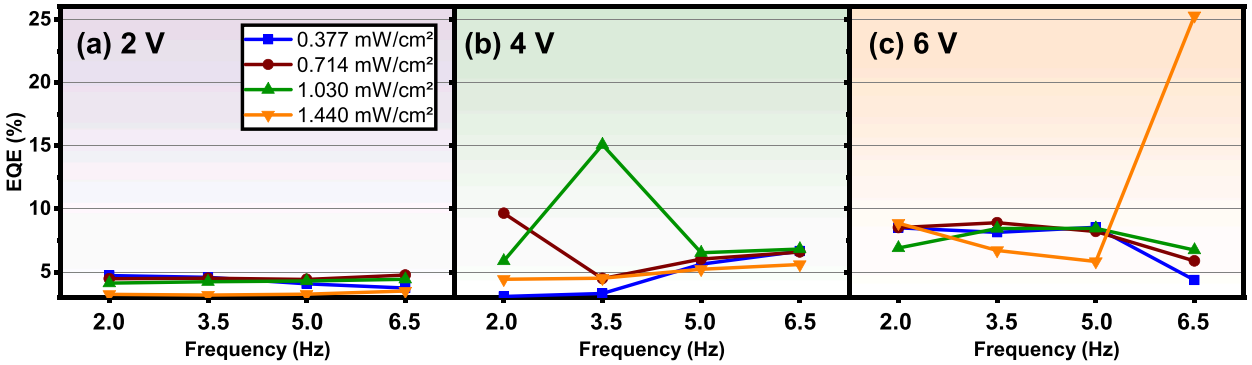

Fig. 9. EQE values for PSi/Ge NPs/ZnO NIR Photodetector under (a) 2, (b) 4, and (c) 6 V bias voltage.

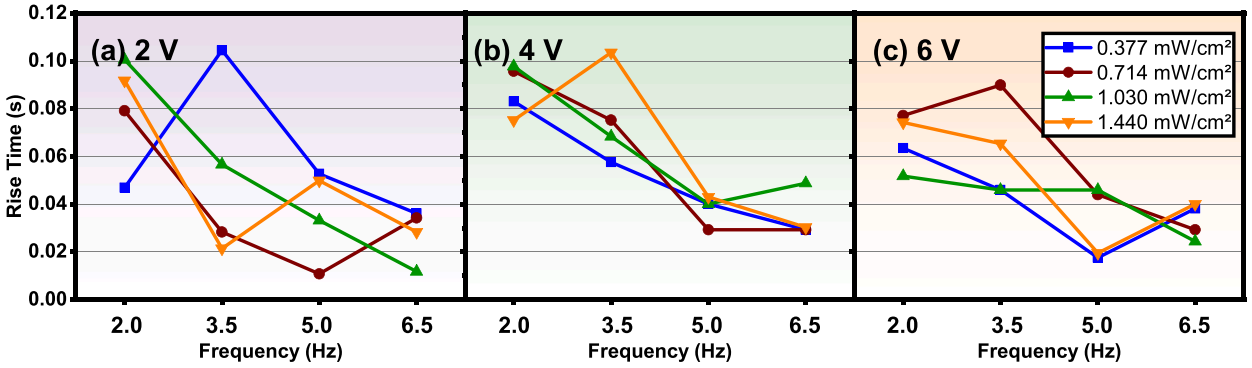

Fig. 10. Rise time values for PSi/Ge NPs/ZnO NIR Photodetector under (a) 2, (b) 4, and (c) 6 V bias voltage.

photocurrent to fall from 90 to 10 % of its maximum photocurrent, when the illumination is switched off [31]. The general trend shows that for all bias voltages, the rise time reduces as the switching frequency increases. The rise time is recorded at 0.05–0.10 s at 2 Hz, reduced to 0.01–0.04 s at 6.5 Hz under 2 V bias voltage. Similar trends are observed for 4 and 6 V respectively. A previous study by Son et al. also showed that the rise time of photodetectors usually becomes shorter as the pulse width (or switching frequency) becomes smaller (or higher) [32].

The bias voltages and illumination intensity do not appear to play a very important role in affecting rise time. For 2, 4, and 6 V bias voltages, the rise time ranges from 0.01 to 0.10 s for all illuminations.

Fig. 11(a–c) shows the fall time for the photodetector under 2, 4, and 6 V bias voltage, plotted with 2–6.5 Hz switching frequency and 0.377–1.440 mW cm^{-2} intensities. Again, an increase in switching frequency resulted in a reduction of fall time, with bias voltage and illumination intensity not providing a direct relationship in affecting fall time.

After the analysis of the photodetector performance, there is a need to understand the various mechanisms present in the photodetector. Fig. 12 shows the energy band diagram of (a) PSi and ZnO and (b) Ge NP and ZnO, at zero bias. A previous study by You

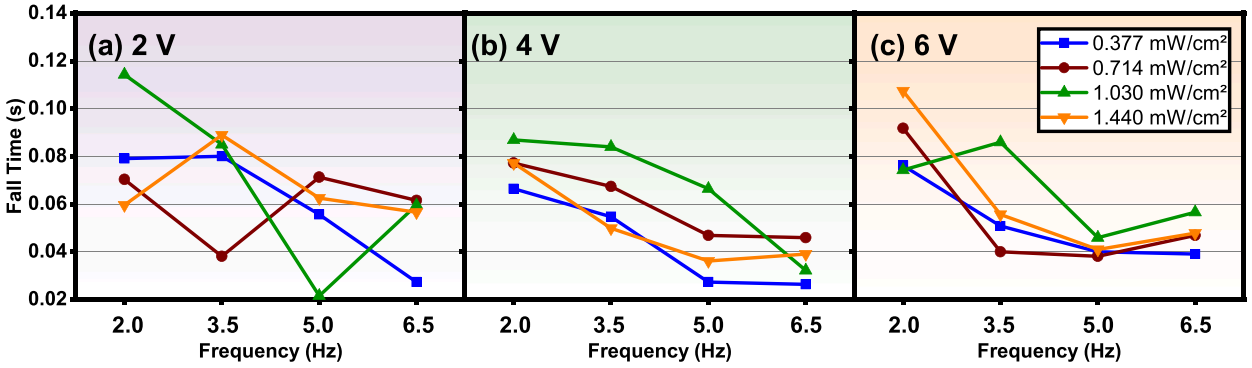

Fig. 11. Fall time values for PSi/Ge NPs/ZnO NIR Photodetector under (a) 2, (b) 4, and (c) 6 V bias voltage.

et al. has elucidated a similar photodetector device, with electrospun disordered ZnO Nanowires/Ge Quantum Dots structure [33]. The ZnO NW/Ge QD structure was fabricated on a Si substrate, and hence the Si substrate plays a role in the photodetector mechanism, which is the same in our work. The band gaps of Si and ZnO are 1.12 eV and 3.37 eV, respectively. This difference leads to a conduction band offset (ΔE_C) of 0.31 eV, favorable for electron transfer from Si to ZnO. Additionally, the valence band offset (ΔE_V) is calculated to be 2.56 eV, promoting hole transfer from ZnO to Si. As illustrated in Fig. 12 (a), this configuration achieves a type-II energy band alignment at the interface. Under near-infrared light illumination, there will be more hole-electron pairs generated in PSi, given the smaller band gap of Si compared to ZnO. The Si/ZnO heterojunction allows efficient separation at the junction due to the internal electric field present. This provides a more efficient source of photoelectrons compared to just the photoconductive nature of Si alone [34]. At forward bias, the energy band of ZnO would be lifted upwards, allowing more flow of electrons. Despite the knowledge that ZnO having a large band gap should be suitable as UV photodetectors, it does not stop researchers from fabricating ZnO/Si heterojunctions for UV–Visible–Near-Infrared ranges [35].

With the introduction of Ge NPs, the Ge NPs act as a source of photogenerated electrons during NIR radiation and thus transfer the photogenerated electrons to the ZnO, with the proposed mechanism shown in Fig. 12 (b). As shown in the FESEM and EDX analysis, the presence of both Ge and ZnO in combination supports this proposition. Like the work of You et al. [33], their Ge QDs have a GeO_xH_y shell, formed during the oxidation and annealing process. This shell has been a cause of reduced photogenerated carriers due to the shell acting as a barrier and causing tunnelling effects [33]. Just like in our work, we can also posit that there would be an oxidation effect due to low-temperature processing during the synthesis of Ge NPs, as shown by EDX results. This could impede the transfer of electrons from Ge to ZnO. However, the additional layer of ZnO deposited by RF sputtering provided further protection against oxidation of the Ge NPs.

It is also important to note the carrier transfer between PSi and Ge NPs. Given that Ge and Si have similar electron affinities [36] ($\chi_{Ge} = 4.0$ eV and $\chi_{Si} = 4.04$ eV) there is a probability of electrons being transferred from Ge to PSi. However, as explained in Fig. 12 (a), the photogenerated electrons in PSi will then be transferred to ZnO. Due to PSi, ZnO, and Ge being crystalline solids, the main charge transfer would be by drift mechanism, with the application of a bias voltage speeding the process [37]. Charge transfer by tunnelling could not be discounted or neglected, as there are interfacial defects present at the interface at PSi/ZnO, PSi/Ge, and ZnO/Ge that would act as small energy barriers and also as space charge regions and thus limit charge transfer by drift mechanism [38], not forgetting the oxidation of Ge NPs. Furthermore, charge transfer by band hopping would be unlikely as that is the main charge transport mechanism for organic or amorphous semiconductors [39].

Looking back at the FESEM analysis in Fig. 2, there was the formation of Ge microwires, before a layer of ZnO deposited onto them and shown in an enlarged version in Fig. 13 (a). Ge nanostructures have been studied and documented on their ability to generate photocarriers after illumination by light. Yan et al. stated that individual Ge nanowires undergo electron conduction by the adsorption and desorption of oxygen molecules [40]. When exposed to air, oxygen atoms attach themselves to the surface of the nanowires (NWs) by capturing electrons. Under light illumination, these captured electrons are freed, generating mobile charge carriers within the NWs. The "holes" left behind by the freed electrons can either migrate to the surface and fill the empty electron traps created by the oxygen atoms, or cause the oxygen atoms themselves to detach from the surface [40].

This mechanism of oxygen and hole diffusion is slow and thus junctions between Ge NWs provided another way to explain the faster response times, via barrier-modulated conduction, which gives a fast rise and fall time. A study by Zhou et al. [41] explored how barriers influence conduction in ZnO nanowires (NWs). They compared the photoresponse of a single ZnO NW with two types of electrical contacts: ohmic contacts (providing low resistance) and Schottky contacts (forming a potential barrier). The NW exhibited a very slow response with ohmic contacts, while its response significantly improved with Schottky contacts.

This difference can be explained by the interplay between oxygen adsorption/desorption and the Schottky barrier. When a Schottky contact is present, the adsorption and desorption of oxygen atoms around the contact area can significantly affect the current flow. Under light illumination, the oxygen desorbs, which increases the number of mobile charge carriers within the NW and reduces the height of the Schottky barrier. This decrease in barrier height allows for a higher current flow, leading to a faster and stronger photoresponse.

Conversely, when the light is turned off, oxygen atoms readily adsorb back onto the NW surface, particularly around the Schottky contact. This adsorption process decreases the number of charge carriers and increases the height of the Schottky barrier. As a result, the current rapidly decreases compared to a ZnO photodetector with an ohmic contact, which lacks the influence of this oxygen-mediated barrier modulation.

In the case of Ge NWs which are in contact with each other, the NW-NW junction provides the barrier-dominated conduction as seen in ZnO NWs. As studied by Aksoy et al. and shown in Fig. 13 (b), the NW-NW junction acts as two Schottky barriers in a back-to-back configuration, due to the oxidation layer surrounding the Ge NW [42]. During light illumination, there will be an increase in carrier density, and thus the NW-NW junction barrier decreases and electron conduction occurs.

In our study, it is proposed that Ge microwires provide the same barrier-dominated conduction for photogenerated electrons. Not only that, the barrier can provide a depletion layer for the separation of photogenerated electrons and holes. The microwires' subsequent contact with ZnO allows the transfer of photogenerated electrons to ZnO, with a similar explanation given for the contact between Ge NP and ZnO in Fig. 12 (b).

To enrich this research work, a table of comparison was prepared in Table 2, showing the performance of Ge photodetectors that have been fabricated by past researchers and some silicon/graphene and CNT/Si photodiodes.

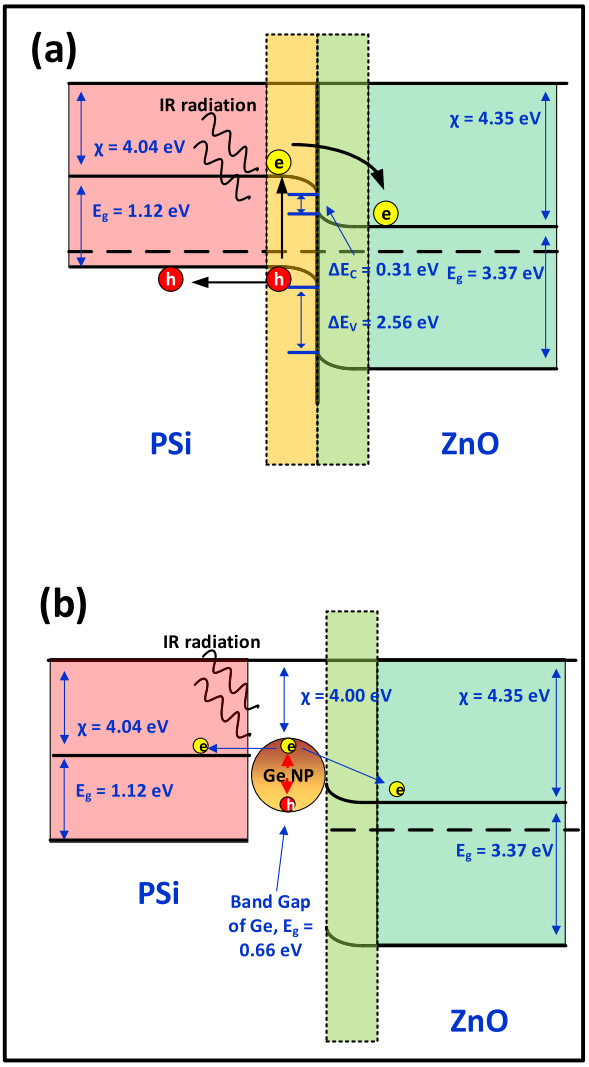

Fig. 12. (a) Energy band diagram of PSi/ZnO and (b) Ge NP/ZnO and Ge NP/PSi.

4. Conclusion

As a conclusion, this work studies the fabrication of ZnO/Ge/porous Si photodetector and its testing properties. The novelty in this work is that the Ge NPs are synthesized via pulsed laser ablation in liquid (PLAL) before being transferred and spray-coated onto porous Si. This is then followed by a deposition of the ZnO layer and electrodes. FESEM analysis showed the presence of Ge NPs. There was a formation of Ge microwires and a Ge mesh-like pattern on the surface of porous Si, due to the supersaturation of Ge NPs during spray coating. For its performance as a photodetector, the device has a configuration of Ag/PSi/Ge/ZnO/Ag and was responsive to 805 nm illumination with various intensities and switching speeds. An increase in light intensity increases sensitivity, however, an increase in bias voltage gives the opposite effect due to an increase in dark current. The increase in bias voltage increases the responsivity of the device, due to a stronger electric field separating photogenerated holes and electrons and a larger depletion region. An increase in illumination switching speed resulted in a decrease in the rise and fall time but does not appear to affect sensitivity and responsivity values. The deposition of Ge NPs and its subsequent microwires formation have played a part in the photodetection mechanisms in the fabricated device. Ge NPs act as a source of photogenerated electrons and are transferred to the ZnO layer. Furthermore, the network of Ge microwires provides barrier-dominated conduction, acting as a source of photogenerated electrons and transfer into the ZnO layer. The device obtained the best performance at 6 V bias voltage (805 nm, 1.44 mW cm^{-2}, 6.5 Hz switching frequency), recording a Responsivity of 0.16 A W^{-1}.

CRediT authorship contribution statement

Mazin Mohd Qasim Mogdad: Writing – original draft, Validation, Methodology, Investigation, Formal analysis, Data curation,

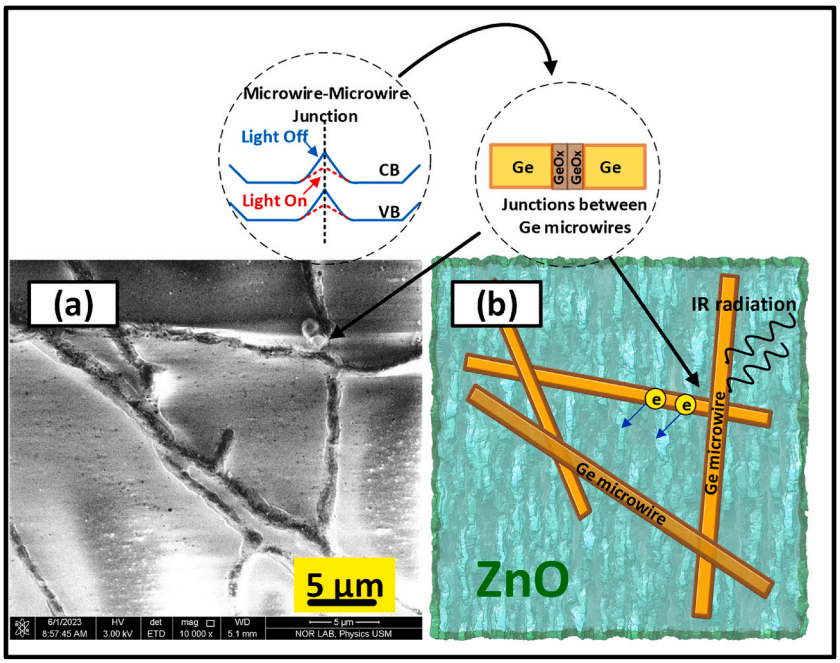

Fig. 13. (a) Enlarged FESEM image of Ge microwires and (b) proposed pathway of photogenerated electrons from Ge microwires to ZnO layer.

Table 2
Table of comparison for the performance of photodetectors by past researchers with our current work.

Photodetector Structure	λ (nm)	Bias Voltage (V)	Light Intensity (mW cm^{-2})	S (%)	R (A/W)	EQE (%)	Ref.
Si/ZnO/Ge	880	−8	–	–	0.172	–	[33]
Si/Ge QDs	1550	–	–	–	0.015	–	[43]
Si/Ge QDs	1550	–	–	–	1.500	–	[44]
Carbon nanotube/Si_3N_4/Si capacitor + PtTi/Si3N4/Si metal–insulator-semiconductor (MIS) diode	950	–	8.00	–	0.370	50	[45]
Schottky Graphene-Si junction in parallel with Graphene-Si_3N_4-Si	500–1200	–	0–240	–	0.350	75	[46]
Multilayer Tungsten disulphide (WS_2) flakes	1250	0	–	–	4.5×10^{-6}	–	[47]
Si/Ge Microwires + NPs/ZnO	805	6	1.44	78	0.160	25	This work

Conceptualization. **Azhar Abdul Rahman:** Writing – review & editing, Visualization, Supervision, Resources, Investigation, Data curation. **Naser M. Ahmed:** Validation, Resources, Project administration, Investigation, Funding acquisition, Data curation. **Suvindraj Rajamanickam:** Writing – review & editing, Validation, Data curation. **Munirah A. Almessiere:** Writing – review & editing, Validation.

Data availability statement

The authors confirm that the data supporting the findings of this study are available within the article [and/or] its supplementary materials.

Declaration of competing interest

The authors declare that they have no known competing financial interests or personal relationships that could have appeared to influence the work reported in this paper.

Acknowledgment

The authors would like to thank the School of Physics at USM University for providing the research facilities and support. We

appreciate the financial support from the RCMO USM through the Short-Term Grant (304/PFIZIK/6315514).

References

[1] K. Gundepudi, P.M. Neelamraju, S. Sangaraju, G.K. Dalapati, W.B. Ball, S. Ghosh, S. Chakrabortty, A review on the role of nanotechnology in the development of near-infrared photodetectors: materials, performance metrics, and potential applications, J. Mater. Sci. 58 (35) (2023) 13889–13924.
[2] Z. Wang, S. Cheng, K. Fukuda, W. Hu, X. Xu, T. Someya, Flexible near-infrared organic photodetectors for emergent wearable applications, Wearable Electr. 1 (2024) 53–77.
[3] Z. Wu, Y. Zhai, H. Kim, J.D. Azoulay, T.N. Ng, Emerging design and characterization guidelines for polymer-based infrared photodetectors, Accounts Chem. Res. 51 (12) (2018) 3144–3153.
[4] R.A. Ismail, A.M. Alwan, A.S. Ahmed, Preparation and characteristics study of nano-porous silicon UV photodetector, Appl. Nanosci. 7 (1) (2017) 9–15.
[5] R.A. Ismail, Fabrication and characterization of photodetector based on porous silicon, e-J. Surf. Sci. Nanotechnol. 8 (2010) 388–391.
[6] U.M. Nayef, K.A. Hubeatir, Z.J. Abdulkareem, Ultraviolet photodetector based on TiO2 nanoparticles/porous silicon heterojunction, Optik 127 (5) (2016) 2806–2810.
[7] X. Liu, X. Ji, M. Liu, N. Liu, Z. Tao, Q. Dai, L. Wei, C. Li, X. Zhang, B. Wang, High-performance Ge quantum dot decorated graphene/zinc-oxide heterostructure infrared photodetector, ACS Appl. Mater. Interfaces 7 (4) (2015) 2452–2458.
[8] H.T. Hussein, M.K.A. Mohammed, R.I. Kamel, U.M. Nayef, Improved sensing performance of porous silicon photodetector with CuO nanoparticles, Chem. Pap. 75 (12) (2021) 6257–6264.
[9] R.A. Ismail, K.S. Khashan, A.M. Alwan, Study of the effect of incorporation of CdS nanoparticles on the porous silicon photodetector, Silicon 9 (3) (2017) 321–326.
[10] D. Mo, L. Hu, G. Zeng, G. Chen, J. Wan, Z. Yu, Z. Huang, K. He, C. Zhang, M. Cheng, Cadmium-containing quantum dots: properties, applications, and toxicity, Appl. Microbiol. Biotechnol. 101 (7) (2017) 2713–2733.
[11] S. Brittman, A.E. Colbert, T.H. Brintlinger, P.D. Cunningham, M.H. Stewart, W.B. Heuer, R.M. Stroud, J.G. Tischler, J.E. Boercker, Effects of a lead chloride shell on lead sulfide quantum dots, J. Phys. Chem. Lett. 10 (8) (2019) 1914–1918.
[12] H.B. Jalali, S. Sadeghi, I.B. Dogru Yuksel, A. Onal, S. Nizamoglu, Past, present and future of indium phosphide quantum dots, Nano Res. 15 (5) (2022) 4468–4489.
[13] K.D. Wegner, S. Pouget, W.L. Ling, M. Carrière, P. Reiss, Gallium – a versatile element for tuning the photoluminescence properties of InP quantum dots, Chem. Commun. 55 (11) (2019) 1663–1666.
[14] S. Prabakar, A. Shiohara, S. Hanada, K. Fujioka, K. Yamamoto, R.D. Tilley, Size controlled synthesis of germanium nanocrystals by hydride reducing agents and their biological applications, Chem. Mater. 22 (2) (2010) 482–486.
[15] S. Vadavalli, S. Valligatla, B. Neelamraju, M.H. Dar, A. Chiasera, M. Ferrari, N.R. Desai, Optical Properties of Germanium Nanoparticles Synthesized by Pulsed Laser Ablation in Acetone, 2, 2014.
[16] J. Liu, C. Liang, Z. Tian, S. Zhang, G. Shao, Spontaneous growth and chemical reduction ability of Ge nanoparticles, Sci. Rep. 3 (1) (2013) 1741.
[17] S.M. Mohammad, N.M. Abd-Alghafour, R.A. Talib, Z. Hassan, N.M. Ahmed, A.A. Abuelsamen, N. Afzal, Influence of growth temperature and duration on different properties of ultra-long ZnO nanorods grown by modified chemical bath deposition method, Mater. Res. Express 5 (9) (2018).
[18] A. Muhammad, Z. Hassan, S.M. Mohammad, S. Rajamanickam, S.M. Abed, M.G.B. Ashiq, Realization of UV-C absorption in ZnO nanostructures using fluorine and silver co-doping, Colloid Interf. Sci. Commun. 47 (2022) 100588.
[19] S. M. Abed, S. M. Mohammad, Z. Hassan, A. Muhammad, S. Rajamanickam, and K. Ali, "Comparative study of UV-ZnO NRs photodetectors based on seeded porous silicon by RF-sputtering and drop-casting methods", J. Mater. Sci. Mater. Electron., vol., 2022.
[20] A. Muhammad, Z. Hassan, S.M. Mohammad, S. Rajamanickam, Enhanced sensitivity of low-cost fabricated fluorine doped ZnO metal semiconductor metal photodetector, Opt. Mater. 122 (2021).
[21] D. Panda, T.-Y. Tseng, One-dimensional ZnO nanostructures: fabrication, optoelectronic properties, and device applications, J. Mater. Sci. 48 (20) (2013) 6849–6877.
[22] L.Z. Pei, Z.Y. Cai, A review on germanium nanowires, Recent Pat. Nanotechnol. 6 (1) (2012) 44–59.
[23] M. Ge, J.F. Liu, H. Wu, C. Yao, Y. Zeng, Z.D. Fu, S.L. Zhang, J.Z. Jiang, Synthesis of germanium nanowires, J. Phys. Chem. C 111 (30) (2007) 11157–11160.
[24] G. Gu, M. Burghard, G.T. Kim, G.S. Düsberg, P.W. Chiu, V. Krstic, S. Roth, W.Q. Han, Growth and electrical transport of germanium nanowires, J. Appl. Phys. 90 (11) (2001) 5747–5751.
[25] Y. Yamada, T. Yamada, A. Shimazaki, A. Wakamiya, Y. Kanemitsu, Interfacial charge-carrier trapping in CH3NH3PbI3-based heterolayered structures revealed by time-resolved photoluminescence spectroscopy, J. Phys. Chem. Lett. 7 (11) (2016) 1972–1977.
[26] P.R. Jubu, F.K. Yam, Development and characterization of MSM UV photodetector based on gallium oxide nanostructures, Sensor Actuator Phys. 312 (2020) 112141.
[27] A. Muhammad, Z. Hassan, S.M. Mohammad, S. Rajamanickam, I.G. Shitu, Fabrication of ultra-violet photodetector with enhanced optoelectronic parameters using low-cost F-doped ZnO nanostructures, Sensor Actuator Phys. 332 (2021) 113092.
[28] S. Rajamanickam, S.M. Mohammad, I.A. Razak, S.M. Abed, A. Muhammad, Comparison study on the influence of pure PFO and PFO-ZnO nanorods in PFO/n-Si photodiodes, J. Polym. Res. 30 (5) (2023) 181.
[29] X. Meng, Y. Du, W. Wu, N.B. Joseph, X. Deng, J. Wang, J. Ma, Z. Shi, B. Liu, Y. Ma, F. Yue, N. Zhong, P.-H. Xiang, C. Zhang, C.-G. Duan, A. Narayan, Z. Sun, J. Chu, X. Yuan, Giant superlinear power dependence of photocurrent based on layered Ta2NiS5 photodetector, Adv. Sci. 10 (20) (2023) 2300413.
[30] D.A. Neamen, McGraw- Hill (Eds.), Semiconductor Physics and Devices, fourth ed., 2003. New York.
[31] B. Deka Boruah, S. Naidu Majji, S. Nandi, A. Misra, Doping controlled pyro-phototronic effect in self-powered zinc oxide photodetector for enhancement of photoresponse, Nanoscale 10 (7) (2018) 3451–3459.
[32] K.T. Son, C.C. Lee, Multiple-target laser rangefinding receiver using a silicon photomultiplier array, IEEE Trans. Instrum. Meas. 59 (11) (2010) 3005–3011.
[33] J. You, Y. Zhang, M. Yang, B. Wang, H. Hu, Z. Wang, J. Li, H. Sun, L. Wang, Ultraviolet-visible-near infrared broadband photodetector based on electronspun disorder ZnO nanowires/Ge quantum dots hybrid structure, Journal 12 (2) (2022).
[34] Z. Zheng, L. Gan, J. Zhang, F. Zhuge, T. Zhai, An enhanced UV–Vis–NIR an d flexible photodetector based on electrospun ZnO nanowire array/PbS quantum dots film heterostructure, Adv. Sci. 4 (3) (2017) 1600316.
[35] G. Chatzigiannakis, A. Jaros, R. Leturcq, J. Jungclaus, T. Voss, S. Gardelis, M. Kandyla, Laser-microstructured ZnO/p-Si photodetector with enhanced and broadband responsivity across the ultraviolet–visible–near-infrared range, ACS Appl. Electron. Mater. 2 (9) (2020) 2819–2828.
[36] Y.M. Haddara, P. Ashburn, D.M. Bagnall, Silicon-germanium: properties, growth and applications, in: S. Kasap, P. Capper (Eds.), Springer Handbook of Electronic and Photonic Materials, Springer International Publishing, Cham, 2017, p. 1, 1.
[37] F.P. Jose, S.R. Achari, M.K. Jayaraj, A.A. Sukumaran, Charge transfer mechanism of AZO-ZnO photoanode based on impedance study for solar cell application, J. Electroanal. Chem. 901 (2021) 115769.
[38] İ. Taşçıoğlu, W.A. Farooq, R. Turan, Ş. Altındal, F. Yakuphanoglu, Charge transport mechanisms and density of interface traps in MnZnO/p-Si diodes, J. Alloys Compd. 590 (2014) 157–161.
[39] H. Geng, Q. Peng, L. Wang, H. Li, Y. Liao, Z. Ma, Z. Shuai, Toward quantitative prediction of charge mobility in organic semiconductors: tunneling enabled hopping model, Adv. Mater. 24 (26) (2012) 3568–3572.
[40] C. Yan, N. Singh, H. Cai, C.L. Gan, P.S. Lee, Network-enhanced photoresponse time of Ge nanowire photodetectors, ACS Appl. Mater. Interfaces 2 (7) (2010) 1794–1797.

[41] J. Zhou, Y. Gu, Y. Hu, W. Mai, P.-H. Yeh, G. Bao, A.K. Sood, D.L. Polla, Z.L. Wang, Gigantic enhancement in response and reset time of ZnO UV nanosensor by utilizing Schottky contact and surface functionalization, Appl. Phys. Lett. 94 (19) (2009) 191103.
[42] B. Aksoy, S. Coskun, S. Kucukyildiz, H.E. Unalan, Transparent, highly flexible, all nanowire network germanium photodetectors, Nanotechnology 23 (32) (2012) 325202.
[43] Y. Zhao, L. Li, S. Liu, J. Wang, J. Xu, Y. Shi, K. Chen, P. Roca i Cabarrocas, L. Yu, Germanium quantum dot infrared photodetectors addressed by self-aligned silicon nanowire electrodes, Nanotechnology 31 (14) (2020) 145602.
[44] S. Siontas, D. Li, H. Wang, A. A.V.P.S, A. Zaslavsky, D. Pacifici, High-performance germanium quantum dot photodetectors in the visible and near infrared, Mater. Sci. Semicond. Process. 92 (2019) 19–27.
[45] A. Pelella, D. Capista, M. Passacantando, E. Faella, A. Grillo, F. Giubileo, N. Martucciello, A. Di Bartolomeo, A self-powered CNT–Si photodetector with tuneable photocurrent, Adv. Electron. Mater. 9 (1) (2023) 2200919.
[46] A. Pelella, A. Grillo, E. Faella, G. Luongo, M.B. Askari, A. Di Bartolomeo, Graphene–silicon device for visible and infrared photodetection, ACS Appl. Mater. Interfaces 13 (40) (2021) 47895–47903.
[47] A. Pelella, K. Intonti, O. Durante, A. Kumar, L. Viscardi, S. De Stefano, P. Romano, F. Giubileo, H. Neill, V. Patil, L. Ansari, B. Roycroft, P.K. Hurley, F. Gity, A. Di Bartolomeo, Multilayer WS2 for low-power visible and near-infrared phototransistors, Discover Nano 19 (1) (2024) 57.